

Article

# Formation of Hydrocarbons in the Presence of Native Iron under Upper Mantle Conditions: Experimental Constraints

Alexander Sokol <sup>1,2,\*</sup>, Anatoly Tomilenko <sup>1</sup>, Ivan Sokol <sup>1</sup>, Pavel Zaikin <sup>3</sup>  and Taras Bul'bak <sup>1</sup>

<sup>1</sup> V.S. Sobolev Institute of Geology and Mineralogy, Siberian Branch of the Russian Academy of Sciences (IGM SB RAS), 3, Koptyug ave., 630090 Novosibirsk, Russia; tomilen@igm.nsc.ru (A.T.); isokol0x5a@gmail.com (I.S.); taras@igm.nsc.ru (T.B.)

<sup>2</sup> Novosibirsk State University, 2, Pirogov str., 630090 Novosibirsk, Russia

<sup>3</sup> N.N. Vorozhtsov Novosibirsk Institute of Organic Chemistry, Siberian Branch of the Russian Academy of Sciences (NIOCh SB RAS), 9, Lavrentiev ave., 630090 Novosibirsk, Russia; zaikin@nioch.nsc.ru

\* Correspondence: sokola@igm.nsc.ru

Received: 10 December 2019; Accepted: 16 January 2020; Published: 21 January 2020



**Abstract:** The formation of hydrocarbons (HCs) upon interaction of metal and metal–carbon phases (solid Fe, Fe<sub>3</sub>C, Fe<sub>7</sub>C<sub>3</sub>, Ni, and liquid Fe–Ni alloys) with or without additional sources of carbon (graphite, diamond, carbonate, and H<sub>2</sub>O–CO<sub>2</sub> fluids) was investigated in quenching experiments at 6.3 GPa and 1000–1400 °C, wherein hydrogen fugacity ( $fH_2$ ) was controlled by the Fe–FeO + H<sub>2</sub>O or Mo–MoO<sub>2</sub> + H<sub>2</sub>O equilibria. The aim of the study was to investigate abiotic generation of hydrocarbons and to characterize the diversity of HC species that form in the presence of Fe/Ni metal phases at P–T– $fH_2$  conditions typical of the upper mantle. The carbon donors were not fully depleted at experimental conditions. The ratio of H<sub>2</sub> ingress and consumption rates depended on hydrogen permeability of the capsule material: runs with low-permeable Au capsules and/or high hydrogenation rates (H<sub>2</sub>O–CO<sub>2</sub> fluid) yielded fluids equilibrated with the final assemblage of solid phases at  $fH_2^{\text{sample}} \leq fH_2^{\text{buffer}}$ . The synthesized quenched fluids contained diverse HC species, predominantly light alkanes. The relative percentages of light alkane species were greater in higher temperature runs. At 1200 °C, light alkanes (C<sub>1</sub> ≈ C<sub>2</sub> > C<sub>3</sub> > C<sub>4</sub>) formed either by direct hydrogenation of Fe<sub>3</sub>C or Fe<sub>7</sub>C<sub>3</sub>, or by hydrogenation of graphite/diamond in the presence of Fe<sub>3</sub>C, Fe<sub>7</sub>C<sub>3</sub>, and a liquid Fe–Ni alloy. The CH<sub>4</sub>/C<sub>2</sub>H<sub>6</sub> ratio in the fluids decreased from 5 to 0.5 with decreasing iron activity and the C fraction increased in the series: Fe–Fe<sub>3</sub>C → Fe<sub>3</sub>C–Fe<sub>7</sub>C<sub>3</sub> → Fe<sub>7</sub>C<sub>3</sub>–graphite → graphite. Fe<sub>3</sub>C–magnesite and Fe<sub>3</sub>C–H<sub>2</sub>O–CO<sub>2</sub> systems at 1200 °C yielded magnesiowüstite and wüstite, respectively, and both produced C-enriched carbide Fe<sub>7</sub>C<sub>3</sub> and mainly light alkanes (C<sub>1</sub> ≈ C<sub>2</sub> > C<sub>3</sub> > C<sub>4</sub>). Thus, reactions of metal phases that simulate the composition of native iron with various carbon donors (graphite, diamond, carbonate, or H<sub>2</sub>O–CO<sub>2</sub> fluid) at the upper mantle P–T conditions and enhanced  $fH_2$  can provide abiotic generation of complex hydrocarbon systems that predominantly contain light alkanes. The conditions favorable for HC formation exist in mantle zones, where slab-derived H<sub>2</sub>O-, CO<sub>2</sub>- and carbonate-bearing fluids interact with metal-saturated mantle.

**Keywords:** mantle; fluid; hydrocarbons; subduction; experiment; native iron; gas chromatography–mass spectrometry

## 1. Introduction

Abiotic hydrocarbons (HCs) have been found in Earth's seafloor hydrothermal systems [1,2], crustal crystalline rocks [3], inclusions of mantle-derived diamonds [4–7], and meteorites [8], as well as on other planets [9]. Abiotic hydrocarbon production on the global scale is minor compared to

hydrocarbon production by microbial processes or thermogenic degradation of organic matter in sedimentary rocks [10]. Yet, HCs that form in reduced mantle may play a key role in the deep cycles of carbon and hydrogen, and facilitate the transport of volatiles to shallow oxidized mantle [11,12]. On the other hand, oxidation of HCs at depths ranging from 150 km to 200 km with the formation of  $\text{H}_2\text{O}$ ,  $\text{C}^0$ , and  $\text{CO}_2$  is favorable for magma generation [11–13] and crystallization of lithospheric diamonds [14,15].

Hydrocarbon genesis in the mantle may potentially occur by hydrolysis or hydrogenation of iron carbides and graphite or diamond, or by reduction of  $\text{CO}$ ,  $\text{CO}_2$ , and carbonates upon reactions with iron compounds and  $\text{H}_2\text{O}$  [10,16–25]. The formation of HCs in the presence of FeO-bearing carbonates and  $\text{H}_2\text{O}$  has received the most exhaustive experimental constraints [16,17,21–23]. The synthesis of HCs under the mantle P–T conditions was inferred [21] to require a donor of carbon (of any type), a donor of hydrogen, and a reducing environment. Specific P–T conditions in the pressure range of 1–11 GPa and temperatures  $\leq 1600$  °C determine the predominant HC species: methane and ethane or natural gas-like mixtures [16,21]. Only at pressures greater than 2.5 GPa, methane transforms into heavier alkanes, and the transformation processes are enhanced at higher temperatures [16]. Heavy hydrocarbon species commonly form in the C–H system at lower mantle pressures and temperatures [26]. Direct hydrogenation of graphite at high  $f\text{H}_2$  yields larger amounts of methane than the reaction of FeO,  $\text{CaCO}_3$ , and  $\text{H}_2\text{O}$  at low  $f\text{H}_2$  [18]. In a previous study [25], we reproduced the formation of HCs at 5.5–7.8 GPa and 1100–1400 °C by reacting hydrogen-bearing fluids with  $^{13}\text{C}$  soot-like carbon, graphite, or diamond as carbon sources.  $^{13}\text{C}$  carbon reacted with hydrogen to yield isotopically pure  $^{13}\text{C}$  light alkanes; the reaction with graphite at 6.3 GPa progressively accelerated and became avalanche-like in runs longer than 1 h; and the use of diamond as a carbon source resulted in HC formation, but at the slowest rate.

Currently, there is a wealth of evidence [11,12,27–31] on settings favorable for abiotic HC generation in the mantle in the presence of carbon and hydrogen donors and a reducing environment. Large amounts of C- and H-bearing species are delivered to the mantle by subducted slabs, which can carry and release  $\text{H}_2\text{O}$ ,  $\text{CO}_2$ , and carbonates as far as the lower mantle [29–32]. The redox conditions in the slab are variable, but generally more oxidized than in the ambient mantle [11,33]. The total amount of water transported to the mantle is estimated to be  $8.7 \times 10^{11}$  kg/year [29], and the subducted mass of  $\text{H}_2\text{O}$  in most slabs is much larger than that of  $\text{CO}_2$  [32,34]. At pressures greater than 5 GPa, the carbonate-bearing sediments yield an  $\text{H}_2\text{O}$ -bearing carbonated melt [35]. Carbonated melts are expected to travel into the mantle due to their low viscosity and good wetting properties [35,36]. The present-day annual subduction input of carbon reaches  $5.4\text{--}8.8 \times 10^{13}$  g [31]. Slab-derived fluids are known to interact with the ambient mantle and cause its metasomatic alteration [37,38].

The decrease in oxygen fugacity with depth is maintained by progressive disproportionation by the reaction  $3\text{Fe}^{2+} \rightarrow 2\text{Fe}^{3+} + \text{Fe}^0$  resulting from a pressure-dependent increase of  $\text{Fe}^{3+}$  stability in silicate phases [28,39], whereby the mantle becomes saturated with native iron [27,28,39,40]. The presence of a metal phase in the upper mantle is evident from inclusions in diamonds that store iron, widespread cogenite ( $\text{Fe}_3\text{C}$ ), and Fe–Ni or Fe–Ni–S alloys [7,41–44]. The metal phase of inclusions in eclogitic diamond commonly contains 0.1–0.5% Ni [42–44], and that in equilibrium with peridotite can contain up to  $X_{\text{Ni}} > 0.5$  [28,39,40,45]. Specifically, at 10 GPa, the contents of Fe-based alloys in peridotite can vary from 50 to 700 ppm, with  $X_{\text{Ni}}$  between 0.34 and 0.58 [40]. Judging by phase relations in the Fe–Ni–C and Fe– $\text{Fe}_3\text{C}$ – $\text{Fe}_3\text{N}$  systems at 7.8–10 GPa and 1350–1475 °C, the dissolution of C and N in amounts typical of the upper mantle can produce assemblages of  $\text{Fe}_3\text{C}$  or  $\text{Fe}_7\text{C}_3$  carbides (with Ni impurity)  $\pm$  metal melt  $\pm$  diamond [40,46]. At greater depths of 600 km, the metal concentration may reach 5000 ppm [39] and carbide  $\text{Fe}_7\text{C}_3$  may gain more importance [40,47].

The penetration of slab-derived fluids or melts into the metal-saturated mantle can induce the  $\text{Fe} + \text{H}_2\text{O} \rightarrow \text{FeO} + \text{H}_2$  reaction [29,48,49] which buffers  $f\text{H}_2$  at the  $\text{IW} + \text{H}_2\text{O}$  (Fe–FeO +  $\text{H}_2\text{O}$ ) equilibrium. This provides a constant source of hydrogen and controls strongly reduced conditions, while the melting of silicates is impeded by “redox freezing” [11,40]. Carbon may come from iron carbides, graphite, or

diamond produced by reactions of Fe-based alloys with carbonate or CO<sub>2</sub> [40,50,51]. Thus, necessary and sufficient conditions for HC generation may arise in the zones of interaction between slab-derived H<sub>2</sub>O–CO<sub>2</sub> fluids or H<sub>2</sub>O-bearing carbonated melts and reduced iron-saturated mantle. The process of abiotic generation of HCs at the mantle P–T–fH<sub>2</sub> conditions upon interaction of iron carbides and an Fe–Ni melt with graphite, diamond, carbonate, and fluids, as well as the speciation of the resulting hydrocarbons, can be investigated in laboratory experiments. For this, we have performed quenching experiments at 6.3 GPa and 1000–1400 °C, which generally reproduce the conditions that typically occur in zones of mantle–slab interaction. Iron carbides, graphite, diamond, magnesite, and CO<sub>2</sub> in fluids were used as carbon donors, while the presence of metal phases maintained strongly reduced conditions in the samples. Hydrogen fugacity was buffered using the double-capsule technique [52] by the IW + H<sub>2</sub>O or MMO + H<sub>2</sub>O (Mo–MoO<sub>2</sub> + H<sub>2</sub>O) equilibria [53]. Thus, more insights were gained into the formation mechanism and speciation of HCs which may originate abiotically upon mantle–slab interaction, and into their fate in the lithospheric mantle.

## 2. Materials and Methods

### 2.1. Materials

Some experiments were prepared by mixing Fe, Ni, or Fe<sub>3</sub>C with graphite (all >99.99% pure; Table 1). The starting iron and nickel powders (10–50 µm) were cleaned from oxygen by annealing for 1 h in a stream of hydrogen at 600 °C. Some amounts of oxides may have formed on metal particles even after cleaning. Graphite pre-dried at 110 °C for at least 30 days contained 700 ppm of CO<sub>2</sub> and 700 ppm of H<sub>2</sub>O. In other experiments, the starting materials included Fe<sub>3</sub>C, natural magnesite (Mg<sub>0.9</sub>Ca<sub>0.1</sub>) CO<sub>3</sub> (Satka, Ural region), chemical-grade oxalic acid (C<sub>2</sub>H<sub>2</sub>O<sub>4</sub>), and synthetic diamond (ACM-20/14, 14–20 µm). Initial Fe<sub>3</sub>C (X-ray tested) was synthesized at 6.3 GPa and 1400 °C from iron and graphite (both >99.99% pure). Samples with low carbon contents were placed in an Al<sub>2</sub>O<sub>3</sub> container with a 0.5 mm inner diameter, which prevented Pt or Au capsules from fusion with iron and/or carbides and thus kept them tight. The use of a graphite container (0.5 mm inner diameter) in the runs with graphite-saturated samples impeded reactions of the capsule material with the metal phases. The Al<sub>2</sub>O<sub>3</sub> and graphite containers, in turn, were placed in Pt or Au capsules with a 2 mm outer diameter and a wall thickness of 0.2 mm and then were arc-welded using a PUK-4U impulse micro welding device (Lampert Werktechnik GmbH, Germany).

Unlike Pt, Au does not show obvious catalytic activity with respect to the HC fluid, but Pt is more permeable to hydrogen than Au and thus can provide the required rate of fH<sub>2</sub> equilibration during buffering. Therefore, Pt capsules were used preferably in most of the runs.

### 2.2. High-Pressure Apparatus

Experiments at 6.3 GPa were carried out in a split-sphere multi-anvil high-pressure apparatus [54]. The size of pressure cells was 21.1 × 21.1 × 25.4 mm; graphite heaters in the high pressure runs had an inner diameter of 12 mm and a height of 18.5 mm. Pressure was calibrated by recording the change in the resistance of Bi at 2.55 GPa and PbSe at 4.0 and 6.8 GPa at room temperature and at 1350 °C by bracketing the graphite–diamond equilibrium in the Ni<sub>0.7</sub>–Fe<sub>0.3</sub>–C system. Temperature was monitored in each experiment with a PtRh6/PtRh30 thermocouple calibrated at 6.3 GPa using the melting points of Al and Ag [55]. See Supplementary Figure S1a,b for the cell layout and the temperature pattern. Pressure and temperature were measured to an accuracy of ±0.1 GPa and ±20 °C, respectively [54,55]; no significant pressure gradients were observed. The run duration of 10–15 h was chosen from our earlier experimental studies [56], in which a system consisting mainly of light alkanes (formed by thermal destruction of docosane and stearic acid) reached equilibrium in 2 h at 6.3 GPa and 1200–1400 °C. The obtained fluids were quenched at 200 deg/s.

**Table 1.** Starting compositions and conditions of 6.3 GPa runs and phase compositions of run products (according to X-ray diffraction analysis and EDS microanalysis).

Run #	Starting Composition (mg)							C (wt.%)	T (°C)	t (hrs)	$f_{H_2}$ Buffer	Capsule	Phase Composition (XRD + EDS)	TIC (Arbitrary Units)
	Gr	Dm	Fe	Ni	Fe <sub>3</sub> C	Mgs	OA							
<i>Samples unsaturated with graphite</i>														
2095_2_2*	0.3	-	4	-	-	-	-	7	1200	10	IW	Pt	Fe + Fe <sub>3</sub> C	$1.23 \times 10^{10}$
2095_2_4*	0.3	-	-	-	4.2	-	-	13	1200	10	IW	Pt	Fe <sub>3</sub> C + Fe <sub>7</sub> C <sub>3</sub>	$1.16 \times 10^{10}$
688_6_2*	-	-	-	-	3.6	1.0	-	11	1200	10	IW	Au	Fe <sub>7</sub> C <sub>3</sub> + Mws + Mws <sub>L</sub>	$3.39 \times 10^9$
688_6_3*	-	-	-	-	2.4	-	0.4	10	1200	10	IW	Au	Fe <sub>7</sub> C <sub>3</sub> + FeO	$3.93 \times 10^{10}$
<i>Samples saturated with graphite</i>														
1079_5_1	7.3	-	-	-	-	-	-	100	800	10	MMO	Pt	Gr	$5.65 \times 10^8$
1079_5_2	10	-	2.4	-	-	-	-	81	800	10	MMO	Pt	Gr + Fe <sub>3</sub> C	$6.28 \times 10^8$
1001_4_3	10	-	-	2.3	-	-	-	81	1000	10	MMO	Pt	Gr + Ni	$4.79 \times 10^{10}$
1001_4_4	10	-	2.1	-	-	-	-	83	1000	10	MMO	Pt	Gr + Fe <sub>3</sub> C	$5.24 \times 10^{10}$
2095_2_3*	1.6	-	-	-	4.2	-	-	67	1200	10	IW	Pt	Gr + Fe <sub>7</sub> C <sub>3</sub>	-
600_8_2	10	-	3.3	1.7	-	-	-	67	1200	15	IW	Pt	Gr + L	$6.63 \times 10^{10}$
600_8_4	6.9	-	-	4.5	-	-	-	61	1200	15	IW	Pt	Gr + Ni	$4.43 \times 10^{10}$
2100_2_2	8.5	-	-	-	8.8	-	-	53	1200	10	IW	Pt	Gr + Fe <sub>7</sub> C <sub>3</sub>	$7.52 \times 10^{10}$
2100_2_3	10.4	-	-	1.5	9.4	-	-	52	1200	10	IW	Pt	Gr + L	$3.95 \times 10^{10}$
2100_2_4*	3	-	-	-	7	-	-	35	1200	10	IW	Pt	Gr + Fe <sub>7</sub> C <sub>3</sub>	$3.39 \times 10^9$
688_6_1*	-	0.3	-	-	4.0	-	-	13	1200	10	IW	Au	Dm + Fe <sub>3</sub> C + Fe <sub>7</sub> C <sub>3</sub> **	$3.69 \times 10^9$
605_8_5	6.8	-	4.6	-	-	-	-	60	1400	15	IW	Pt	Gr + L	$1.4 \times 10^9$
605_8_7	6.6	-	1.6	3.3	-	-	-	57	1400	15	IW	Pt	Gr + L	$2.09 \times 10^8$
605_8_8	6.8	-	-	4.5	-	-	-	60	1400	15	IW	Pt	Gr + L	$1.08 \times 10^9$

\* Samples placed in Al<sub>2</sub>O<sub>3</sub> container; other samples were placed in graphite containers; \*\* unequilibrated assemblage. Gr = graphite; Dm = diamond; Mgs = magnesite; OA = oxalic acid (C<sub>2</sub>H<sub>2</sub>O<sub>4</sub>); L = quenched liquid; Mws = magnesiowüstite; Mws<sub>L</sub> = quenched magnesiowüstite. TIC = total ion count obtained by GC-MS, which semi-quantitatively characterizes the amount of fluid in the capsule after the run.

The presence of Fe and iron carbides buffered  $f_{O_2}$  in the samples within IW ( $\Delta \log f_{O_2}$  FMQ-5). Hydrogen fugacity was controlled by the IW + H<sub>2</sub>O (Fe–FeO + H<sub>2</sub>O) and slightly more oxidized MMO + H<sub>2</sub>O (Mo–MoO<sub>2</sub> + H<sub>2</sub>O) buffers (MMO =  $\Delta \log f_{O_2}$  IW + 1 [53]). A double-capsule technique was used: inner Pt capsules were placed inside thick-walled Fe or Mo outer capsules with talc as a source of water and low-melting CsCl insulation which maintained quasi-hydrostatic pressure transfer (Supplementary Figure S1). The precipitation of FeO and MoO<sub>2</sub> on the inner walls of the outer capsules after the experiments was confirmed by X-ray analysis. The procedure was previously described in detail in [25,53,56].

### 2.3. Analytical Methods

After retrieval from the high-pressure cells, the Pt and Au capsules were placed into a crush cell connected on-line to a gas chromatograph before the analytical column. They were heated at 120–130 °C in a stream of carrier gas (99.9999% pure He) for 90 min to clean the surface from adsorbed gases and to evaporate water for further analysis of the released gases. The duration of pre-heating depended on the rate of gas desorption and was analyzed on-line. The blank pre-heating runs showed neither speciation nor concentration changes of volatiles in the capsules at 120–130 °C. The capsules that did not sustain heating were excluded from the analysis. The gas mixture extracted from the capsules by piercing was analyzed by gas chromatography and mass spectrometry using a Focus GS/DSQ II Series Single Quadrupole MS analyzer (Thermo Fischer Scientific, Waltham, MA, USA) [56]. Gas samples were not pyrolyzed and the analysis was thus applied to an almost in situ gas mixture. Trace amounts of poorly volatile components of the quenched fluids, especially heavy hydrocarbons (>C<sub>18</sub>), remained in the capsules.

According to our estimates [25], HC formation by hydrogenation of graphite and diamond in the 5.5–7.8 GPa and 1100–1400 °C runs increased the fluid in the capsules by 3 to 100 times relative to the amount prior to experiments. In this study, total ion count (TIC) was used to semi-quantitatively characterize the amount of fluid in the capsule after the run. The relative concentrations (rel.%) of volatile components in the studied mixture were obtained by normalization: the total area of all

chromatographic peaks was normalized to 100% and the area of an individual component defined its proportion in the mixture (Supplementary Figures S2 and S3). The normalization quality was checked against external standards [56]. The concentration ranges of alkanes during the calibration were the same as in the run products. Analytical uncertainty was below 5% for C<sub>1</sub>–C<sub>4</sub> alkanes and less than 10% for H<sub>2</sub>O, NH<sub>3</sub>, and CO<sub>2</sub> (determined in the range from 12.5 pptv to 12.5 ppbv and expressed as precision), or even less than 5% in most cases.

The samples retrieved from the capsules were mounted in an epoxy resin by vacuum impregnation. After resin polymerization, the samples were polished under kerosene, without the use of water (final stage: 1 µm Al<sub>2</sub>O<sub>3</sub>) and examined on a MIRA 3 LMU scanning electron microscope (SEM) (Tescan, Brno, Czech Republic). For quantitative determination, metal phases were analyzed on the Tescan MIRA 3 LMU scanning electron microscope coupled with an INCA EDS 450 microanalysis system with a liquid nitrogen-free large area EDS X-Max-80 Silicon Drift Detector (Oxford Instruments Nanoanalysis Ltd., Oxford, UK). The instruments were operated at an accelerating voltage of 20 kV, a beam current of 1 nA, and a spot diameter of ~10 nm; and the counting time was 20 s.

The phases were identified by X-ray powder diffraction on an IPDS-2T diffractometer (Stoe & Cie GmbH, Darmstadt, Germany) in the Gandolfi mode (MoK $\alpha$  radiation, graphite monochromator). Two-dimensional X-ray patterns were radially integrated using the XArea software package. The diffraction profiles were processed in WinXPow (Stoe & Cie GmbH, Darmstadt, Germany). The database of PDF-4 Minerals (Powder Diffraction File PDF-4+, 2006) was used for phase analysis.

### 3. Results

#### 3.1. Phase Relations

The phase composition of run products was reconstructed using scanning electron microscopy coupled with EDS microanalysis and X-ray powder diffraction (Tables 1 and 2; Figure 1; Supplementary Figure S4). In the course of the experiment, the samples became either saturated or unsaturated with respect to graphite/diamond (Table 1). The C-unsaturated samples contained  $\leq 13$  wt % C, while graphite from the starting mixture disappeared, as it was confirmed by X-ray and SEM data. Most likely it was dissolved in metal phases early during the runs and formed iron carbides which underwent hydrogenation to produce HCs. At 1200 °C, the carbon-deficient run (2095\_2\_2) yielded Fe<sub>3</sub>C (93.0 wt % Fe) and Fe (Tables 1 and 2; Figure 1a; Supplementary Figure S4c), but the carbides Fe<sub>3</sub>C (92.4 wt % Fe) and Fe<sub>7</sub>C<sub>3</sub> (90.4 wt % Fe) formed at higher C contents in runs 2095\_2\_4 (Tables 1 and 2; Figure 1b). The run 688\_6\_1 was likely unequilibrated, judging by the association of diamond with two carbides, Fe<sub>3</sub>C and Fe<sub>7</sub>C<sub>3</sub>.

**Table 2.** Chemistry of metal phases according to EDS microanalysis (wt %).

Run #	n	Phase	Fe	1 $\sigma$	Ni	1 $\sigma$	O	1 $\sigma$	Mg	1 $\sigma$	Pt	1 $\sigma$	Total
2095_2_2	5	Fe	99.0	0.4	-	-	-	-	-	-	-	-	99.0
2095_2_2	5	Fe <sub>3</sub> C	93.0	0.4	-	-	-	-	-	-	-	-	93.0
2095_2_4	15	Fe <sub>3</sub> C	92.4	0.4	-	-	-	-	-	-	-	-	92.4
2095_2_4	6	Fe <sub>7</sub> C <sub>3</sub>	90.4	0.4	-	-	-	-	-	-	-	-	90.4
688_6_2	8	Fe <sub>7</sub> C <sub>3</sub>	90.3	0.4	-	-	-	-	-	-	-	-	90.3
688_6_2	8	Mws	62.6	0.6	-	-	24.7	0.5	11.7	0.3	-	-	99.0
688_6_2	9	Mws <sub>L</sub>	63.8	2.7	-	-	26.0	1.5	11.2	1.1	-	-	101.0
1079_5_2	7	Fe <sub>3</sub> C	92.5	0.4	-	-	-	-	-	-	-	-	92.5
1001_4_3	7	Ni	-	-	99.7	0.2	-	-	-	-	-	-	99.7
1001_4_4	8	Fe <sub>3</sub> C	92.7	0.5	-	-	-	-	-	-	-	-	92.7
1001_4_4	6	FeO	78.9	0.6	-	-	22.1	0.5	-	-	-	-	100.9
2095_2_3	6	Fe <sub>7</sub> C <sub>3</sub>	90.6	0.4	-	-	-	-	-	-	-	-	90.6
600_8_2	7	L	65.8	0.8	29.1	0.6	-	-	-	-	1.8	0.5	96.7
600_8_4	5	Ni	-	-	99.3	0.7	-	-	-	-	-	-	99.3
2100_2_2	8	Fe <sub>3</sub> C	91.1	0.1	-	-	-	-	-	-	-	-	91.1
2100_2_3	6	L	73.1	0.2	15.4	0.5	-	-	-	-	7.2	0.4	95.7
2100_2_4	6	Fe <sub>7</sub> C <sub>3</sub>	90.6	0.4	-	-	-	-	-	-	-	-	90.6
688_6_1	8	Fe <sub>3</sub> C	92.7	0.3	-	-	-	-	-	-	-	-	92.7
688_6_1	7	Fe <sub>7</sub> C <sub>3</sub>	90.2	0.4	-	-	-	-	-	-	-	-	90.2
688_6_3	7	Fe <sub>7</sub> C <sub>3</sub>	90.3	0.3	-	-	-	-	-	-	-	-	90.3
688_6_3	9	FeO	77.8	0.3	-	-	23.2	0.3	-	-	-	-	101.0
605_8_5	7	L	79.4	0.2	-	-	-	-	-	-	16.3	0.8	95.6
605_8_5	8	FeO	76.6	0.2	-	-	21.9	0.5	-	-	-	-	98.5
605_8_7	6	L	26.2	0.5	47.8	1.1	-	-	-	-	25.9	1.6	99.9
605_8_8	9	L	-	-	49.8	0.1	0.6	0.1	-	-	50.1	0.7	100.5

n = Number of analyses averaged to obtain the reported composition; 1 $\sigma$  = standard deviation; L = quenched liquid; Mws = magnesiowüstite; Mws<sub>L</sub> = quenched magnesiowüstite.

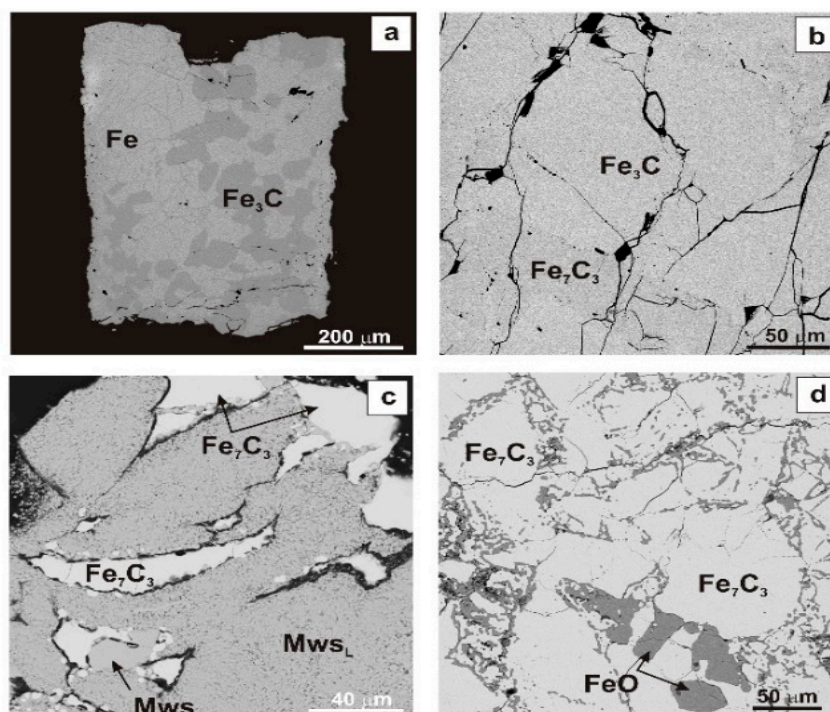


**Figure 1.** Backscattered electron (BSE) images of quenched samples after 6.3 GPa and 1200 °C runs. (a) run 2095\_2\_2 (Pt capsule); (b) run 2095\_2\_4 (Pt capsule); (c) run 688\_2\_2 (Au capsule); (d) run 688\_2\_3 (Au capsule).

In other 1200 °C runs with graphite/diamond-unsaturated samples (688\_6\_2 and 688\_6\_3), reactions of Fe<sub>3</sub>C with magnesite or oxalic acid yielded assemblages of Fe<sub>7</sub>C<sub>3</sub> (90.3 wt % Fe) with magnesiowüstite (18–20 wt % MgO) or wüstite (Figure 1c,d). As indicated by the sample texture, a large part of magnesiowüstite was molten, but the EDS microanalysis showed almost identical compositions of solid and quenched magnesiowüstite (Table 2). The carbon-saturated systems produced graphite and Fe<sub>3</sub>C with 91.1–92.7 wt % Fe at 800 °C and 1000 °C (Tables 1 and 2; Supplementary Figure S4b), but a higher-C carbide Fe<sub>7</sub>C<sub>3</sub> with 90.4–90.6 wt % Fe at 1200 °C (Supplementary Figure S4d). The 1000 °C and 1200 °C runs with Ni-bearing and C-saturated samples yielded nickel and graphite (Supplementary Figure S4a).

The metal phases (some obtained at 1200 °C and all from 1400 °C runs; Table 1) had particular textures due to dendritic crystals. These crystals may be produced by melt quenching, as evidenced by published experimental results for Fe–Ni–C–N systems at mantle P–T conditions [40,47,57]. Melting was observed in a 1200 °C run with the graphite–Fe–Ni system (Fe/(Fe + Ni) weight ratios of 0.5 and 0.75) and in 1400 °C runs with the graphite–Fe, graphite–Ni, and graphite–Fe–Ni (Fe/(Fe + Ni) = 0.2) systems (Table 1). The EDS microanalysis revealed Pt contamination of the molten metal, which increased with temperature (1.8–7 wt % Pt at 1200 °C and 16–50 wt % Pt at 1400 °C). The graphite–Fe, graphite–Fe<sub>3</sub>C, and graphite–Ni samples were free from Pt in the 800 °C to 1200 °C runs, when no melting occurred.

### 3.2. Species in Quenched Fluids

Fluids equilibrated with solid or liquid metal phases were present in the run products at all T–*f*H<sub>2</sub> conditions, and their compositions were analyzed by the GC-MS method. The fluid phase was distributed along grain boundaries within the crystalline matrix. The fluids appeared quenched upon capsule opening and consisted of species that are gaseous or liquid under normal conditions. Our previous results [56,58,59], along with published data [16,21,48], confirmed that the applied 200 deg/s quenching rate prevents any inverse reaction and ensures preservation of species till the GC-MS analysis.

As we showed previously [25], the fluid with high contents of N<sub>2</sub>, CO<sub>2</sub>, and H<sub>2</sub>O formed a few minutes after the graphite-rich system had achieved the target pressure and temperature, on account of species adsorbed on graphite or air entrapped in the welded capsules. The fluid composition did not change in long runs in the absence of external *f*H<sub>2</sub> buffering [25]. The quenched fluid that formed in 10-h 800 °C runs was rich in nitrogen and carbon dioxide despite the MMO + H<sub>2</sub>O buffering of *f*H<sub>2</sub>: 32–63 rel.% N<sub>2</sub>, 15–20 rel.% CO<sub>2</sub>, and 14–16 rel.% H<sub>2</sub>O (Supplementary Table S1; Figure 2). Therefore, the double-capsule technique for *f*H<sub>2</sub> buffering failed at 6.3 GPa and 800 °C. Judging by the high N<sub>2</sub> in quenched fluid after the run at 6.3 GPa and 800 °C with the graphite + Fe system, the nitrogen entrapped from air dissolved neither in the Fe<sup>0</sup> phase nor in graphite.

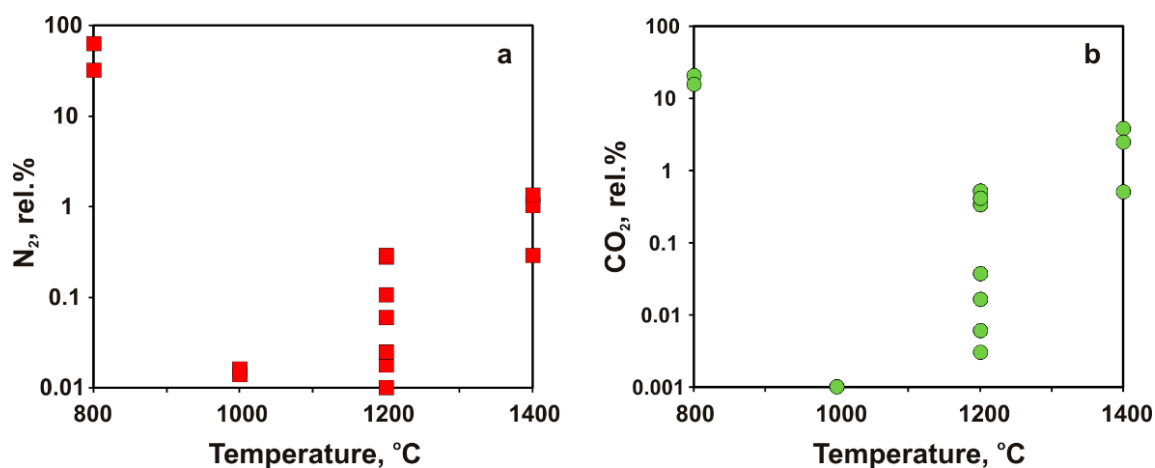


**Figure 2.** Concentrations of (a) N<sub>2</sub> and (b) CO<sub>2</sub> in quenched fluids obtained in 800–1400 °C runs.

The quenched fluids obtained at a higher temperature of 1000 °C had markedly different compositions (Supplementary Table S1; Figures 2–6), with N<sub>2</sub> and CO<sub>2</sub> < 5 rel.%. This could be attributed to the almost complete reduction of CO<sub>2</sub> adsorbed on graphite by hydrogen at buffered  $fH_2$ , N<sub>2</sub> dilution with newly formed HCs, and the formation of other N-bearing species [25,56,59]. Thus, the  $fH_2$  buffering technique worked well at 1000 °C; at higher temperatures, the contents of N<sub>2</sub> and CO<sub>2</sub> increased slightly and exceeded 5 rel.% only at 1400 °C (Figure 2). The CO<sub>2</sub> increase was due to the temperature-dependent decrease in the oxygen affinity of Mo and Fe and the corresponding decrease of buffered  $fH_2$ . As calculated previously [25], the MMO + H<sub>2</sub>O-buffered  $fH_2$  became 0.4 log unit lower at 6.3 GPa as the temperature increased from 1100 °C to 1400 °C. To balance the  $fH_2$  decrease, a slightly more reduced IW + H<sub>2</sub>O buffer was used instead of MMO + H<sub>2</sub>O. The fluids obtained in the 800 °C runs appeared to be equilibrated under unbuffered conditions because the buffer did not work properly at this temperature. The quenched fluids that formed in C-saturated systems at 1000 °C consisted mainly of light alkanes (C<sub>2</sub> > C<sub>3</sub> > C<sub>4</sub> > C<sub>1</sub>), predominantly those heavier than methane (Supplementary Table S1; Figure 4); C<sub>5</sub>H<sub>12</sub> was no more than a few percent, while heavier alkanes were vanishing. The graphite–Fe<sub>3</sub>C and graphite–Ni systems produced almost identical species at 1000 °C.

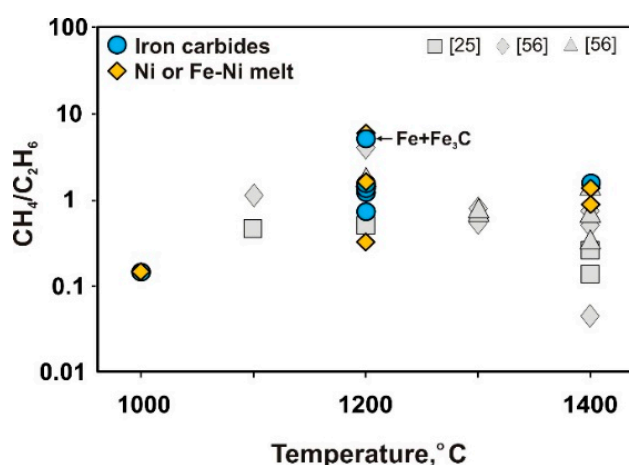


**Figure 3.** CH<sub>4</sub>/C<sub>2</sub>H<sub>6</sub> ratio in quenched fluids obtained in this study by interaction of metal phases with different carbon sources (blue circles and yellow diamonds) and in previous studies [25,56] by thermal destruction of docosane (gray diamonds) or stearic acid (triangles), and by hydrogenation of graphite (squares).

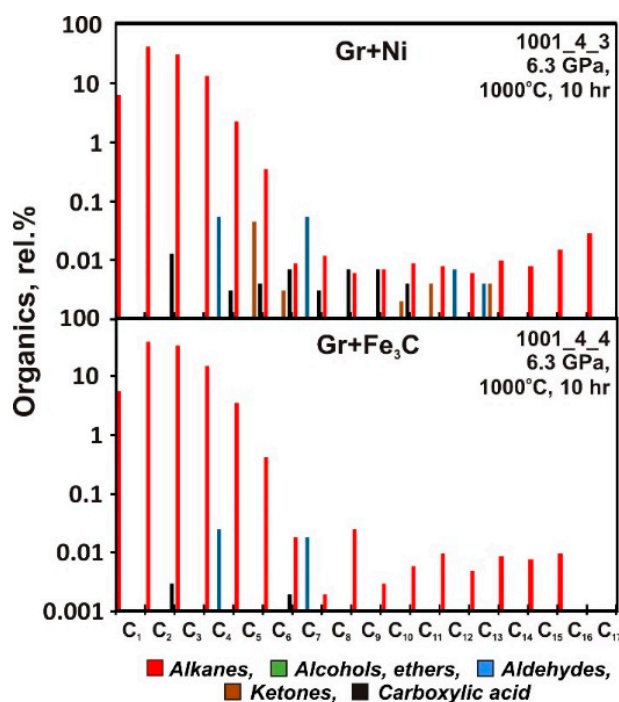


**Figure 4.** Speciation of minor organic components in quenched fluids obtained in 1000 °C runs in the presence of Ni and Fe<sub>3</sub>C.

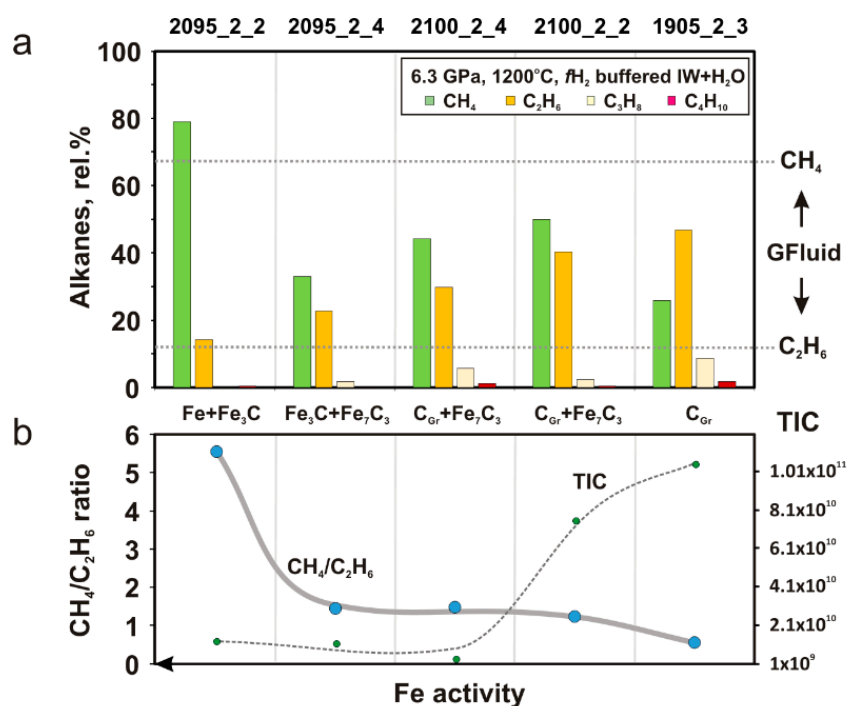


**Figure 5.** (a) Contents of light alkanes C<sub>1</sub>–C<sub>4</sub> and CH<sub>4</sub>/C<sub>2</sub>H<sub>6</sub> ratio in quenched fluids obtained at 1200 °C in samples with buffered Fe and C activity in Pt capsules. Data on run 1905\_2\_3 are from [25]. CH<sub>4</sub> and C<sub>2</sub>H<sub>6</sub> contents calculated with GFluid [60] on the right are shown for comparison. (b) TIC (total ion count) values obtained by GC-MS on the right characterize semi-quantitatively the amount of fluid in the capsule after the run.

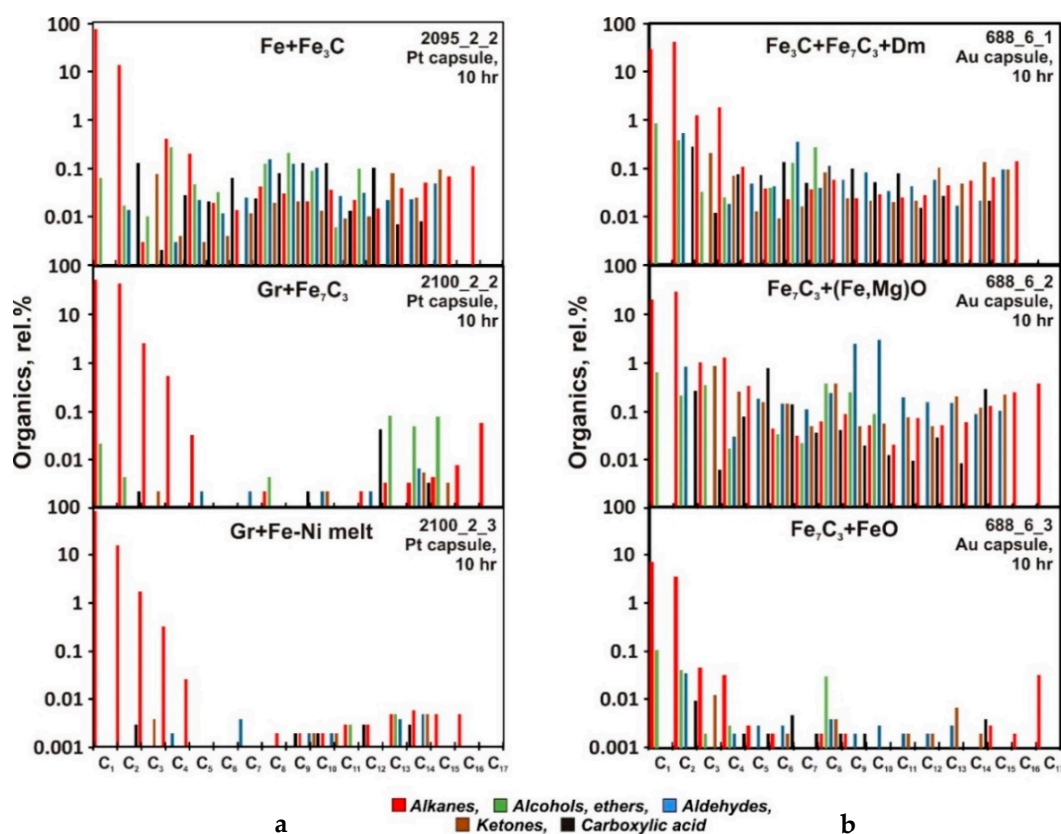


**Figure 6.** Speciation of minor organic components in quenched fluids obtained in the presence of metal phases at 1200 °C. (a) Pt capsules; (b) Au capsules.

The quenched fluids obtained at 1200 °C in Pt capsules consisted mainly of C<sub>1</sub>–C<sub>4</sub> alkanes, but their relative contents differed from the respective values of lower temperature runs (Figures 3–6; Supplementary Table S1; Supplementary Figure S2). The systems including an Fe–Fe<sub>3</sub>C mixture or an Fe–Ni melt yielded fluids with up to 80 rel.% CH<sub>4</sub>, <20 rel.% C<sub>2</sub>H<sub>6</sub>, less than a few percent of other alkanes, and up to 0.1 rel.% of O-bearing species (runs 2095\_2\_2 and 2100\_2\_3, respectively; Figures 5 and 6). Similar alkane species, but with 35–50 rel.% CH<sub>4</sub> and 20–40 rel.% C<sub>2</sub>H<sub>6</sub>, formed from the systems with graphite plus Fe<sub>3</sub>C, Fe<sub>7</sub>C<sub>3</sub>, and Fe<sub>7</sub>C<sub>3</sub> or only Fe<sub>7</sub>C<sub>3</sub>. The fluid synthesized from the graphite–Ni system predominantly contained C<sub>2</sub>H<sub>6</sub> (C<sub>2</sub> > C<sub>1</sub> > C<sub>3</sub> > C<sub>4</sub>) and was compositionally similar to that obtained earlier by hydrogenation of metal-free graphite at the same P–T conditions [25].

The quenched fluids from the non-equilibrium assemblage Dm + Fe<sub>3</sub>C + Fe<sub>7</sub>C<sub>3</sub> obtained at 1200 °C in Au capsules predominantly contained C<sub>2</sub>H<sub>6</sub> (C<sub>2</sub> > C<sub>1</sub> > C<sub>3</sub> ≈ C<sub>4</sub>) and, especially, quite a large amount (0.1–1.0 rel.%) of O-bearing species (run 688\_8\_1; Figure 6). A similar fluid composition containing predominantly C<sub>2</sub>H<sub>6</sub> and high contents of O-bearing species resulted from Fe<sub>3</sub>C interaction with magnesite in an Au capsule (run 688\_8\_2; Figure 6). The reaction of Fe<sub>3</sub>C with an H<sub>2</sub>O–CO<sub>2</sub> fluid in an Au capsule (run 688\_8\_3; Figure 6) yielded quite a different composition: predominantly H<sub>2</sub>O, no more than 10 rel.% of alkanes, and CH<sub>4</sub> exceeding C<sub>2</sub>H<sub>6</sub>. The quenched fluids produced by reactions with oxidized magnesite and a H<sub>2</sub>O–CO<sub>2</sub> fluid contained 1.3 and 0.01 rel.% CO<sub>2</sub>, respectively (Supplementary Table S1).

The fluids that resulted from 1400 °C runs were in equilibrium with Pt-bearing melts and showed the same speciation trends as revealed in the 1200 °C runs. The HC species included predominant light alkanes (Supplementary Table S1; Figure 4), with CH<sub>4</sub> decreasing as C<sub>2</sub>H<sub>6</sub> increased, while the melt composition changed successively as Fe(–Pt) → Ni–Fe(–Pt) → Ni(–Pt). The quenched fluids obtained at 1000–1400 °C contained from tenth fractions of percent to 2 rel.% CH<sub>3</sub>N and NH<sub>3</sub> as main nitrogen species (Supplementary Table S1). In our previous study [25], the amounts of HCs in quenched fluids

were inferred from the degree of atmospheric N dilution with newly formed species. Yet, the approach is inapplicable to this study as nitrogen in Fe-bearing systems can bind efficiently with both Fe<sup>0</sup> and iron carbides by the reaction  $\text{Fe}_3\text{C} + \text{N}_{\text{Fl}} \rightarrow \text{Fe}_3\text{N} + \text{C}_{\text{Gr,Dm}}$ , at the applied P–T conditions [58].

## 4. Discussion

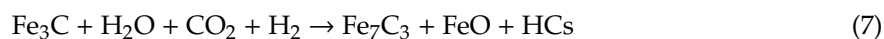
### 4.1. Formation of Hydrocarbons in the Presence of a Metal Phase

The results of experiments at 6.3 GPa and 1000–1400 °C with buffered  $f\text{H}_2$  highlighted the speciation of HCs produced by hydrogenation of Fe + Fe<sub>3</sub>C and Fe<sub>3</sub>C + Fe<sub>7</sub>C<sub>3</sub> in systems unsaturated with respect to graphite/diamond and in C-saturated systems of graphite with Fe<sub>3</sub>C, Fe<sub>7</sub>C<sub>3</sub>, and an Fe–Ni alloy.

Hydrogen fugacity in Pt and Au capsules was controlled by the reactions:



The obtained data have implications for the mechanism of HC generation in the mantle upon interaction between native iron and carbon-bearing phases (graphite, diamond, carbonate, and fluids) at buffered  $f\text{H}_2$ . With the diverse samples used in the experiments, it was possible to reproduce the initial HC formation via hydrogenation:



At the applied P–T conditions, the fluid compositions in the capsules became readily equilibrated due to high rates of the reactions [24]. Several non-catalytic [25] and catalytic processes led to redistribution of the HCs, *vide infra*.

Note that, according to the TIC values obtained by GC-MS (Supplementary Table S1), the amount of fluid synthesized in Pt capsules from graphite was greater than in the case of Au capsules and C-poor systems like Fe–carbide, due to lower hydrogen permeability of gold and lower activity of carbon in C-poor systems (e.g., 2095\_2\_2). Low contents of light hydrocarbons <C<sub>5</sub> in the gas mixture allowed the detection of all minor species with higher relative abundances (Figure 6). The gold capsules, which are less permeable for hydrogen than the platinum ones, may keep  $f\text{H}_2$  below the buffered value at high rates of H<sub>2</sub> consumption. Therefore, the Au capsule runs typically yielded fluids equilibrated with  $f\text{H}_2^{\text{sample}} < f\text{H}_2^{\text{buffer}}$ , and their amount was substantially smaller than that in the Pt capsules. The systems producing little fluid (Au capsules, Fe + Fe<sub>3</sub>C) contained the background composition of minor organic compounds (Figure 6).

In all runs, HCs formed from the available carbon sources: graphite/diamond, carbides, CO<sub>2</sub>, carbonate, or any combination thereof. As Fe<sub>3</sub>C converted to C-enriched Fe<sub>7</sub>C<sub>3</sub>, most of carbon came from magnesite, which reduced to magnesiowüstite either by H<sub>2</sub> or by partial Fe<sub>3</sub>C oxidation, while Fe<sub>3</sub>C oxidation provided additional C inputs to the system. The run products obtained with the Fe<sub>3</sub>C and MgCO<sub>3</sub> proportion used in the study were free from graphite/diamond, possibly, because all excess carbon was reduced at buffered  $f\text{H}_2$ . The formation of graphite and diamond by Fe<sub>3</sub>C oxidation and by Fe<sub>3</sub>C reactions with carbonate was reproduced in previous experiments [50,61,62]. Excess carbon required for HC formation and Fe<sub>3</sub>C-to-Fe<sub>7</sub>C<sub>3</sub> conversion appeared in reaction 7 on account of Fe<sub>3</sub>C oxidation and CO<sub>2</sub> reduction by hydrogen. The hydrogenation of Fe<sub>3</sub>C–Fe<sub>7</sub>C<sub>3</sub> or Fe<sub>3</sub>C–graphite

systems at 6.3 GPa and 1200 °C in Pt capsules (reactions 4 and 5) produced fluids with the  $C_1 > C_2 > C_3 > C_4$  distribution of alkanes. The  $CH_4/C_2H_6$  ratio in the fluids decreased from 5 to 0.5 as the iron activity decreased and the C fraction increased in the series: Fe–Fe<sub>3</sub>C → Fe<sub>3</sub>C–Fe<sub>7</sub>C<sub>3</sub> → Fe<sub>7</sub>C<sub>3</sub>–graphite → graphite (Figure 5). In the presence of iron and carbides,  $fO_2$  was about the IW buffer and thus caused no influence on speciation of HCs in the fluid. The fluid obtained by hydrogenation of graphite in the presence of solid Ni had strongly predominant C<sub>2</sub>H<sub>6</sub> ( $C_2 > C_1 > C_3 > C_4$ ), but the one synthesized in the presence of an Fe–Ni melt (reaction 3) was rich in CH<sub>4</sub>, while the fraction of Ni was minor. The fluid that formed at 1200 °C in an Au capsule in the system with diamond, Fe<sub>3</sub>C, and Fe<sub>7</sub>C<sub>3</sub> (reaction 5) contained commensurate amounts of CH<sub>4</sub> and C<sub>2</sub>H<sub>6</sub> (Figure 6). A similar fluid composition was obtained in an Au capsule by the interaction of Fe<sub>3</sub>C with magnesite (reaction 6). The interaction of Fe<sub>3</sub>C with a H<sub>2</sub>O–CO<sub>2</sub> fluid (reaction 7) in an Au capsule produced an aqueous fluid predominantly containing CH<sub>4</sub>. The relative amounts of alkane species from lower temperature 1000 °C runs with Fe<sub>3</sub>C and Ni were different from those at 1200 °C:  $C_2 > C_3 > C_4 > C_1$ . In general, as the temperature increased from 1000 °C to 1400 °C, the overall alkane composition became lighter (Figure 3).

Previously, we reported that HC fluids obtained by hydrogenation of graphite at high pressures and temperatures in Pt capsules had low methane/ethane ratios [25]; a similar observation was also reported for HC fluids synthesized from graphite with docosane and/or stearic acid [56]. We tentatively attributed the shift toward lower  $CH_4/C_2H_6$  ratios to Pt-promoted radical methane condensation [62]. Similar processes may occur in the presence of supported metal Pt catalysts of alkane homologization, which was described in detail in [63]. The 6.3 GPa and 1200 °C runs in Pt capsules in the presence of Fe<sub>3</sub>C and/or Fe<sub>7</sub>C<sub>3</sub> produced lighter alkanes ( $C_1 > C_2 > C_3 > C_4$ ), while a methane-enriched alkane mixture (up to 80 rel.% CH<sub>4</sub>) was obtained in the C-unsaturated Fe–Fe<sub>3</sub>C system, with iron carbide being the only carbon source. The hydrogenation of graphite in the presence of an Ni-poor Fe–Ni melt also yielded a lighter HC composition. At the same time, alkanes formed by hydrogenation of graphite were similar, despite the presence of solid Ni, and showed typical Pt-related distribution ( $C_2 > C_1 > C_3 > C_4$ ), i.e., solid Ni appeared not to influence the speciation of alkanes. Similar distribution was obtained in the presence of an Ni-poor Fe–Ni melt.

Previously, we reported that HC fluids obtained by hydrogenation of graphite at high pressures and temperatures in Pt capsules had low methane/ethane ratios [25]; a similar observation was also reported for HC fluids synthesized from graphite with docosane and/or stearic acid [56]. We tentatively attributed the shift toward lower  $CH_4/C_2H_6$  ratios to Pt-promoted radical methane condensation [62]. Similar processes may occur in the presence of supported metal Pt catalysts of alkane homologization, which was described in detail in [63]. The 6.3 GPa and 1200 °C runs in Pt capsules in the presence of Fe<sub>3</sub>C and/or Fe<sub>7</sub>C<sub>3</sub> produced lighter alkanes ( $C_1 > C_2 > C_3 > C_4$ ), while a methane-enriched alkane mixture (up to 80 rel.% CH<sub>4</sub>) was obtained in the C-unsaturated Fe–Fe<sub>3</sub>C system, with iron carbide being the only carbon source. The hydrogenation of graphite in the presence of an Ni-poor Fe–Ni melt also yielded a lighter HC composition. At the same time, alkanes formed by hydrogenation of graphite were similar, despite the presence of solid Ni, and showed typical Pt-related distribution ( $C_2 > C_1 > C_3 > C_4$ ), i.e., solid Ni appeared not to influence the speciation of alkanes. Similar distribution was obtained in the presence of an Ni-poor Fe–Ni melt.

The  $CH_4/C_2H_6$  ratios in the experimental Fe-rich systems approached those in C–O–H fluids estimated using the GFluid model [60] for 6.3 GPa and 1200 °C (Figure 5): CH<sub>4</sub> in the latter was either close to or slightly higher than the experimental values, while C<sub>2</sub>H<sub>6</sub> was most often lower. Some other models, e.g., Deep Earth Water (DEW) [64], may be applicable to further research as they allow calculating the compositions of fluids equilibrated with solid phases.

Right after the H<sub>2</sub> buffer starts working, the Pt surface rapidly saturates with adsorbed hydrogen. Methane generated by carbon hydrogenation adsorbs dissociatively onto the inner surface of the Pt capsule, with the formation of methyl species. As their surface concentration increases, the methyl species recombines to produce ethane that desorbs to the fluid. Since the capsule surface is covered with adsorbed hydrogen at the applied run conditions, methane adsorption may require quite a

high methane fugacity to compete with the hydrogen. An increase in Fe loading decreased the available amount of carbon and, hence, the volume of fluid generated by carbon hydrogenation (Figure 5). Low methane fugacity may lead to a shift in the methane adsorption equilibrium and a lower surface concentration of methyl species and related ethane production. The methane/ethane ratio was substantially high at low amounts of fluid produced in runs 2095\_2\_2 and 2095\_2\_4, due to a pronounced effect of metallic Fe. It was also relatively high in run 600\_8\_2, which yielded a high-methane fluid and an Fe–Ni melt, while the amount of fluid was greater than that in 2095\_2\_4 ( $6.6 \times 10^{10}$  against  $1.23 \times 10^{10}$ , according to TIC). Thus, metal phases having high Fe contents increase the methane/ethane ratio of equilibrated fluids. The mechanism may be similar to that reported by Cimino et al. [65] and involves catalytic hydrogenation-cracking. While the distribution of  $\text{CH}_4/\text{C}_2\text{H}_6$  shifted from that predicted by GFluid toward ethane in the absence of Fe-rich metal phases, fluids contained light hydrocarbons in a ratio close to thermodynamically predicted in the presence of Fe-rich metal phases.

#### 4.2. Interaction of Slab-Derived Fluids with Metal-Saturated Mantle

The most advanced of the existing models explains the origin of hydrocarbons in the upper mantle by interaction between FeO-bearing carbonates and  $\text{H}_2\text{O}$  under moderately reduced conditions of  $f\text{O}_2$  near the WM ( $\text{FeO}-\text{Fe}_3\text{O}_4$ ) equilibrium [16,17,21–23]. We suggest a new model which provides insights into the formation of HCs during the interaction of slab-derived fluids with metal-saturated mantle and into their fate in the shallow mantle. With this model, it became possible, for the first time, to evaluate the volume and duration of mantle HC generation in the context of global geodynamic evolution.

The available geochemical, petrological, and experimental data provide solid proof that downgoing slabs transport aqueous fluids with variable amounts of  $\text{CO}_2$  and carbonate into the transition zone and lower mantle [29,31,32,34]. Therefore, slab-derived fluids may penetrate into reduced metal-saturated mantle regions and induce reaction 1 which buffers  $f\text{H}_2$  at the  $\text{IW} + \text{H}_2\text{O}$  equilibrium in the zones of mantle–slab interaction [29,48,49].  $\text{C}^0$  in these zones may result from the reaction of Fe-based alloys with carbonate or  $\text{CO}_2$  [40,50] or reactions 6 and 7 of our study. Thus, slab-derived fluids interact with the mantle under conditions that are necessary and sufficient for HC generation as reproduced in our experiments: the presence of iron (Fe,  $\text{Fe}_3\text{C}$ ,  $\text{Fe}_7\text{C}_3$ , and Fe–Ni alloy) and carbon donors (iron carbides, graphite, diamond, carbonate, or  $\text{H}_2\text{O}-\text{CO}_2$  fluids), as well as enhanced hydrogen fugacity (Figure 7). Heat flux in subcratonic mantle ranges commonly from 35 to 40  $\text{mW}/\text{m}^2$  [66,67] and corresponds to temperatures of  $-1200$  to  $-1450$  °C at a depth of 300 km, while the slab temperatures about this depth may be below 1000 °C [67]. Thus, the temperatures in the mantle–slab interaction zones may range from  $-1000$  to  $-1400$  °C.

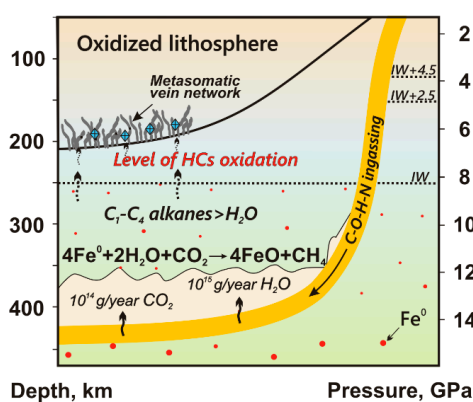


**Figure 7.** Formation of light alkanes in the zone of interaction between slab-derived oxidized volatiles and  $\text{Fe}^0$ -bearing mantle. Black arrows show paths and relative magnitudes of volatile fluxes [29,31].  $\text{IW}$  ( $\text{Fe}-\text{FeO}$  buffer),  $\text{IW} + 2.5$  log units, and  $\text{IW} + 4.5$  log units are  $f\text{O}_2$  values according to [13]. Metasomatic vein network is according to [68]. Blue rhombs are mark diamonds.

Summing up the experimentally reproduced reactions 1 and 3–7, we infer that HCs can form in the zones of mantle–slab interaction by the simplified reaction:



If all  $\text{Fe}^0$  becomes consumed, the input of the following  $\text{H}_2\text{O}$  and  $\text{CO}_2$  batches from the subduction zone can provide  $f\text{O}_2$  increase in the zone of mantle–slab interaction. Wüstite or magnesiowüstite resulting from this interaction may become dissolved in silicate minerals. In a short time,  $f\text{O}_2$  may reach values within the so-called water maximum (carbon-saturated maximum  $\text{H}_2\text{O}$  content for C–O–H fluids, CW) at an oxidation degree of  $\text{IW} + 2.5$  to  $\text{IW} + 4$  log units (the limit of  $\text{C}^0$  stability) [11]. Rapid  $f\text{O}_2$  increase and  $f\text{H}_2$  decrease under the effect of slab-derived fluids in this zone can reduce the yield of HCs, but their generation will hardly stop completely [16,17,21,23].

Thus, the suggested scenario of large-scale HC generation during mantle–slab interaction obviously could work in the very beginning of subduction, when oceanic crust and lithosphere reached the depths of metal-saturated mantle and could be brief on the scale of geological processes. Irreversible binding of oxygen associated with  $f\text{O}_2$  increase in the interaction zone could lead to a brief oxygen decrease in the Earth's atmosphere of that time.

#### 4.3. Fate of HCs in Shallow Mantle

Hydrocarbons, being poorly soluble in silicates, can ascend to shallow mantle with other fluid components, including Mg-, Si-, and Na-bearing organic species [30]. While ascending, such fluids can interact with the ambient peridotite, a typical mantle rock at these depths. The available data on xenoliths indicate a gradual  $f\text{O}_2$  increase from  $-220$  km to the crustal base [11,13,28]. According to experimental results and thermodynamic calculations, rapid oxidation of HCs should occur at  $<200$  km where  $f\text{O}_2$  is near the CW level, and the forming water-rich fluids can bear some HC species [11,14,56,69,70]. The effect of  $\text{H}_2\text{O}$ - and HC-bearing fluids on subcratonic lithosphere can induce its metasomatism with the liberation of quite abundant  $\text{C}^0$  as diamond or graphite [71–73]. For instance, the effect of  $\text{H}_2\text{O}$ – $\text{CH}_4$  fluids may be responsible for the formation of MARID-type veins within the lower reaches of the North Atlantic cratonic lithosphere before approximately 1400 Ma (presumably during the Paleoproterozoic era) [68]. A later redox change, shortly prior and subsequently to approximately 610 Ma, may have led to the injection of oxidized low-degree  $\text{CO}_2$ -rich convective mantle-derived melts into the pre-existing, more reduced, cratonic vein network. The isotope fractionation factor of carbon ( $\Delta\text{C}_{\text{diamond-fluid}}$ ) indicates that partial oxidation of methane-bearing fluids and release of  $\text{C}^0$  can maintain the crystallization of diamond [14,71].

The reactions of fluids with lithospheric peridotite at depths of 150–200 km at  $f\text{O}_2$  corresponding to the EMOD (enstatite-magnesite-olivine-diamond) equilibrium produce  $\text{CO}_2$ -rich fluids/melts [13], which can contain minor amounts of alkanes, alkenes, and O-bearing organic species [70]. Thus, migration of deep HCs should mainly lead to their complete oxidation within the lithospheric mantle. The amount of HCs that the lithospheric mantle can oxidize remains unknown. According to the estimates of Stachel and Luth [14], depleted lithospheric peridotites have quite low buffer capacity, and the  $f\text{O}_2$  change from IW to EMOD on account of bulk  $\text{Fe}^{3+}/\Sigma\text{Fe}$  would require fluid transport of  $<5$  mg  $\text{O}_2$  per 100 g of rock.

## 5. Conclusions

Thus, we have demonstrated that HCs, predominantly light alkanes ( $\text{C}_1 \approx \text{C}_2 > \text{C}_3 > \text{C}_4$ ), can form upon interaction of metal and metal–carbon phases (solid Fe,  $\text{Fe}_3\text{C}$ ,  $\text{Fe}_7\text{C}_3$ , Ni, and liquid Fe–Ni alloys) with or without additional sources of carbon (graphite, diamond, carbonate, and  $\text{H}_2\text{O}$ – $\text{CO}_2$  fluids) at 6.3 GPa and 1000–1400 °C and relatively high  $f\text{H}_2$ . This is experimental proof that the HC generation mechanism can work in the zones of interaction between metal-saturated mantle and slab-derived fluids/melts. The amount of metal phases available for the reaction with volatiles in these zones is small

relative to those of water and carbon subducted annually to the mantle. The oxidation of all Fe<sup>0</sup> to FeO by slab-derived fluids and cessation of large-scale HC generation may occur within a geologically short time span. The existence of a highly oxidized mantle at depths of 150–200 km indicates that HCs generated in reduced mantle can be oxidized completely in the lithosphere.

**Supplementary Materials:** The following are available online at <http://www.mdpi.com/2075-163X/10/2/88/s1>, Table S1: Compositions of quenched fluid. Figure S1: (a) The high-pressure cell; (b) temperature patterns in furnace assembly predicted using the software of Hernlund et al. [74]; (c) the double-capsule technique used to constrain the *f*H<sub>2</sub> conditions by the assemblage Fe + FeO + H<sub>2</sub>O buffer. Figure S2: Results of GC-MS analysis of quenched fluid extracted by mechanical shock destruction from run 2095\_2\_4. Figure S3: Results of GC-MS analysis of quenched fluid extracted by mechanical shock destruction from run 2095\_2\_4. Figure S4: Phases identified by X-ray powder diffraction in the Gandolfi mode.

**Author Contributions:** Conceptualization, A.S. and I.S.; formal analysis, A.S., A.T. and T.B.; investigation, A.S., A.T. and P.Z.; methodology, A.S., A.T. and I.S.; supervision, A.S., A.T. and I.S.; writing—original draft, A.S. and I.S.; writing—review and editing, A.S. and I.S. All authors have read and agreed to the published version of the manuscript.

**Funding:** This work was supported by the Russian Science Foundation under Grant No. 16-17-10041.

**Acknowledgments:** We wish to thank Yuri Palyanov and Yuri Borzdov for their assistance throughout the study.

**Conflicts of Interest:** The authors declare no conflict of interest.

## References

1. Horita, J.; Berndt, M.E. Abiogenic methane formation and isotopic fractionation under hydrothermal conditions. *Science* **1999**, *285*, 1055–1057. [[CrossRef](#)]
2. Etiop, G.; Schoell, M.; Hosgormez, H. Abiotic methane flux from the Chimaera seep and Tekirova ophiolites (Turkey): Understanding gas exhalation from low temperature serpentinization and implications for Mars. *Earth Planet. Sci. Lett.* **2011**, *310*, 96–104. [[CrossRef](#)]
3. Chukanov, N.V.; Pekov, I.V.; Sokolov, S.V.; Nekrasov, A.N.; Chukanova, V.N.; Naumova, I.S. On the problem of the formation and geochemical role of bituminous matter in pegmatites of the Khibiny and Lovozero alkaline massifs, Kola Peninsula, Russia. *Geochem. Int.* **2006**, *44*, 715–728. [[CrossRef](#)]
4. Sobolev, N.V.; Sobolev, A.V.; Tomilenko, A.A.; Kuz'min, D.V.; Grakhanov, S.A.; Batanova, V.G.; Logvinova, A.M.; Bul'bak, T.A.; Kostrovitskii, S.I.; Yakovlev, D.A.; et al. Prospects of search for diamondiferous kimberlites in the northeastern Siberian Platform. *Russ. Geol. Geophys.* **2018**, *59*, 1365–1379. [[CrossRef](#)]
5. Sobolev, N.V.; Tomilenko, A.A.; Bul'bak, T.A.; Logvinova, A.M. Composition of volatile components in the diamonds, associated garnet and olivine from diamondiferous peridotites from the Udachnaya pipe, Yakutia, Russia (by coupled gas chromatographic-mass spectrometric analysis). *Engineering* **2019**, *5*. [[CrossRef](#)]
6. Sobolev, N.V.; Logvinova, A.M.; Tomilenko, A.A.; Wirth, R.; Bul'bak, T.A.; Luk'yanova, L.I.; Fedorova, E.N.; Reutsky, V.N.; Efimova, E.S. Mineral and fluid inclusions in diamonds from the Urals placers, Russia: Evidence for solid molecular N<sub>2</sub> and hydrocarbons in fluid inclusions. *Geochim. Cosmochim. Acta* **2019**, *266*, 197–219. [[CrossRef](#)]
7. Smith, E.M.; Shirey, S.B.; Nestola, F.; Bullock, E.S.; Wang, J.; Richardson, S.H.; Wang, W. Large gem diamonds from metallic liquid in Earth's deep mantle. *Science* **2016**, *354*, 1403–1405. [[CrossRef](#)]
8. Yuen, G.; Blair, N.; Des Marais, D.J.; Chang, S. Carbon isotope composition of low molecular weight hydrocarbons and monocarboxylic acids from Murchison meteorite. *Nature* **1984**, *307*, 252–254. [[CrossRef](#)]
9. Mumma, M.J.; Villanueva, G.L.; Novak, R.E.; Hewagama, T.; Bonev, B.P.; DiSanti, M.A.; Mandell, A.M.; Smith, M.D. Strong release of methane on Mars in northern summer 2003. *Science* **2009**, *323*, 1041–1045. [[CrossRef](#)]
10. Etiop, G.; Sherwood Lollar, B. Abiotic methane on Earth. *Rev. Geophys.* **2013**, *51*, 276–299. [[CrossRef](#)]
11. Foley, S. A reappraisal of redox melting in the Earth's mantle as a function of tectonic setting and time. *J. Petrol.* **2011**, *52*, 1363–1391. [[CrossRef](#)]
12. Luth, R.W. Volatiles in Earth's mantle. In *Treatise on Geochemistry*; Elsevier: Oxford, UK, 2014; Volume 3, pp. 355–391.
13. Stagno, V.; Ojwang, D.O.; McCammon, C.A.; Frost, D.J. The oxidation state of the mantle and the extraction. *Nature* **2013**, *493*, 84. [[CrossRef](#)]

14. Stachel, T.; Luth, R.W. Diamond formation—Where, when and how? *Lithos* **2015**, *220*, 200–220. [[CrossRef](#)]
15. Stagno, V.; Cerantola, V.; Aulbach, S.; Lobanov, S.; McCammon, C.A.; Merlini, M. Carbon-bearing phases throughout Earth's interior—Evolution through space and time. In *Deep Carbon: Past to Present*; Orcutt, B., Daniel, I., Dasgupta, R., Eds.; Cambridge University Press: Cambridge, UK, 2019; pp. 66–88.
16. Kenney, J.F.; Kutcherov, V.A.; Bendeliani, N.A.; Alekseev, V.A. The evolution of multicomponent systems at high pressures: The thermodynamic stability of the hydrogen-carbon system: The genesis of hydrocarbons and the origin of petroleum. *Proc. Nat. Acad. Sci. USA* **2002**, *99*, 10976–10981. [[CrossRef](#)]
17. Scott, H.P.; Hemley, R.J.; Mao, H.; Herschbach, D.R.; Fried, L.E.; Howard, W.M.; Bastea, S. Generation of methane in the Earth's mantle: In situ high pressure–temperature measurements of carbonate reduction. *Proc. Nat. Acad. Sci. USA* **2004**, *101*, 14023–14026. [[CrossRef](#)]
18. Sharma, A.; Cody, G.D.; Hemley, R.J. In situ diamond-anvil cell observations of methanogenesis at high pressures and temperatures. *Energy Fuels* **2009**, *23*, 5571–5579. [[CrossRef](#)]
19. Kolesnikov, A.; Kutcherov, V.G.; Goncharov, A.F. Methane-derived hydrocarbons produced under upper-mantle conditions. *Nat. Geosci.* **2009**, *2*, 566–570. [[CrossRef](#)]
20. Palyanov, Y.N.; Borzdov, Y.M.; Kupriyanov, I.N.; Khokhryakov, A.F. Effect of H<sub>2</sub>O on diamond crystal growth in metal–carbon systems. *Cryst. Growth Des.* **2010**, *12*, 5571–5578. [[CrossRef](#)]
21. Kolesnikov, A.Y.; Saul, J.M.; Kutcherov, V.G. Chemistry of hydrocarbons under extreme thermobaric conditions. *Chem. Sel.* **2017**, *2*, 1336–1352. [[CrossRef](#)]
22. Mukhina, E.; Kolesnikov, A.; Kutcherov, V. The lower pT limit of deep hydrocarbon synthesis by CaCO<sub>3</sub> aqueous reduction. *Sci. Rep.* **2017**, *7*, 5749. [[CrossRef](#)]
23. Tao, R.; Zhang, L.; Tian, M.; Zhu, J.; Liu, X.; Liu, J.; Höfer, H.E.; Stagno, V.; Fei, Y. Formation of abiotic hydrocarbon from reduction of carbonate in subduction zones: Constraints from petrological observation and experimental simulation. *Geochim. Cosmochim. Acta* **2018**, *239*, 390–408. [[CrossRef](#)]
24. Matveev, S.; Ballhaus, C.; Fricke, K.; Truckenbrodt, J.; Ziegenben, D. Volatiles in the Earth's mantle: I. Synthesis of CHO fluids at 1273 K and 2.4 GPa. *Geochim. Cosmochim. Acta* **1997**, *61*, 3081–3088. [[CrossRef](#)]
25. Sokol, A.G.; Tomilenko, A.A.; Bul'bak, T.A.; Sokol, I.A.; Zaikin, P.A.; Palyanova, G.A.; Palyanov, Y.N. Hydrogenation of carbon at 5.5–7.8 GPa and 1100–1400 °C: Implications to formation of hydrocarbons in reduced mantles of terrestrial planets. *Phys. Earth Planet. Inter.* **2019**, *291*, 12–23. [[CrossRef](#)]
26. Lobanov, S.S.; Chen, P.N.; Chen, X.J.; Zha, C.S.; Litasov, K.D.; Mao, H.K.; Goncharov, A.F. Carbon precipitation from heavy hydrocarbon fluid in deep planetary interiors. *Nat. Commun.* **2013**, *4*, 2446. [[CrossRef](#)]
27. Frost, D.J.; Liebske, C.; Langenhorst, F.; McCammon, C.A.; Tronnes, R.G.; Rubie, D.C. Experimental evidence for the existence of iron-rich metal in the Earth's lower mantle. *Nature* **2004**, *248*, 409–412. [[CrossRef](#)]
28. Frost, D.J.; McCammon, C.A. The redox state of Earth's mantle. *Annu. Rev. Earth Planet. Sci.* **2008**, *36*, 389–420. [[CrossRef](#)]
29. Ohtani, E. Water in the mantle. *Elements* **2005**, *1*, 25–30. [[CrossRef](#)]
30. Manning, C.E. Thermodynamic modeling of fluid-rock interaction at mid-crustal to upper-mantle conditions. *Rev. Mineral. Geochem.* **2013**, *76*, 135–164. [[CrossRef](#)]
31. Dasgupta, R. Ingassing, storage, and outgassing of terrestrial carbon through geologic time. *Rev. Mineral. Geochem.* **2013**, *75*, 183–229. [[CrossRef](#)]
32. Plank, T.; Langmuir, C.H. The chemical composition of subducting sediment and its consequences for the crust and mantle. *Chem. Geol.* **1998**, *145*, 325–394. [[CrossRef](#)]
33. Song, S.; Su, L.; Niu, Y.; Lai, Y.; Zhang, L. CH<sub>4</sub> inclusions in orogenic harzburgite: Evidence for reduced slab fluids and implication for redox melting in mantle wedge. *Geochim. Cosmochim. Acta* **2009**, *73*, 1737–1754. [[CrossRef](#)]
34. Rea, D.K.; Ruff, L.J. Composition and mass flux of sediment entering the world's subduction zones: Implications for global sediment budgets, great earthquakes, and volcanism. *Earth Planet. Sci. Lett.* **1996**, *140*, 1–12. [[CrossRef](#)]
35. Schmidt, M.; Poli, S. Devolatilization during subduction. In *Treatise on Geochemistry*, 2nd ed.; Elsevier Science: Oxford, UK, 2014; pp. 669–701.
36. Stagno, V.; Stopponi, V.; Kono, Y.; Manning, C.; Irifune, T. Experimental determination of the viscosity of Na<sub>2</sub>CO<sub>3</sub> melt between 1.7 and 4.6 GPa at 1200–1700 °C: Implications for the rheology of carbonatite magmas in the Earth's upper mantle. *Chem. Geol.* **2018**, *501*, 19–25. [[CrossRef](#)]

37. Pearson, D.G.; Canil, D.; Shirey, S.B. Mantle samples included in volcanic rocks: Xenoliths and diamonds. *Treatise Geochem.* **2003**, *2*, 568.
38. Pearson, D.G.; Wittig, N. The Formation and Evolution of Cratonic Mantle Lithosphere—Evidence from Mantle Xenoliths. In *Treatise on Geochemistry*, 2nd ed.; Elsevier Science: Oxford, UK, 2014; Volume 3, pp. 255–292.
39. Rohrbach, A.; Schmidt, M.W. Redox freezing and melting in the Earth's deep mantle resulting from carbon-iron redox coupling. *Nature* **2011**, *472*, 209. [[CrossRef](#)]
40. Rohrbach, A.; Ghosh, S.; Schmidt, M.W.; Wijbrans, C.H.; Klemme, S. The stability of Fe–Ni carbides in the Earth's mantle: Evidence for a low Fe–Ni–C melt fraction in the deep mantle. *Earth Planet. Sci. Lett.* **2014**, *388*, 211–221. [[CrossRef](#)]
41. Sobolev, N.V.; Efimova, E.S.; Pospelova, L.N. Native iron in Yakutian diamonds and its mineral assemblage. *Sov. Geol. Geophys.* **1981**, *22*, 25–28.
42. Stachel, T.; Harris, J.W.; Brey, G.P. Rare and unusual mineral inclusions in diamonds from Mwadui, Tanzania. *Contrib. Mineral. Petrol.* **1998**, *132*, 34–47. [[CrossRef](#)]
43. Jacob, D.E.; Kronz, A.; Viljoen, K.S. Cohenite, native iron and troilite inclusions in garnets from polycrystalline diamond aggregates. *Contrib. Mineral. Petrol.* **2004**, *146*, 566–576. [[CrossRef](#)]
44. Kaminsky, F.V.; Wirth, R. Iron carbide inclusions in lower-mantle diamond from Juina, Brazil. *Canad. Mineral.* **2011**, *49*, 555–572. [[CrossRef](#)]
45. O'Neill, H.S.C.; Wall, V.J. The Olivine-Orthopyroxene-Spinel oxygen geobarometer, the nickel precipitation curve, and the oxygen fugacity of the Earth's Upper Mantle. *J. Petrol.* **1987**, *28*, 1169–1191. [[CrossRef](#)]
46. Sokol, A.G.; Kruk, A.N.; Seryotkin, Y.V.; Korablin, A.A.; Palyanov, Y.N. Phase relations in the Fe–Fe<sub>3</sub>C–Fe<sub>3</sub>N system at 7.8 GPa and 1350 °C: Implications for carbon and nitrogen hosts in Fe<sub>0</sub>-saturated upper mantle. *Phys. Earth Planet. Inter.* **2017**, *265*, 43–53. [[CrossRef](#)]
47. Lord, O.T.; Walter, M.J.; Dasgupta, R.; Walker, D.; Clark, S.M. Melting in the Fe–C system to 70 GPa. *Earth Planet. Sci. Lett.* **2009**, *284*, 157–167. [[CrossRef](#)]
48. Kutcherov, V.G.; Kolesnikov, A.Y.; Dyuzheva, T.I.; Kulikova, L.F.; Nikolaev, N.N.; Sazanova, O.A.; Braghkin, V.V. Synthesis of Complex Hydrocarbon Systems at Temperatures and Pressures Corresponding to the Earth's Upper Mantle Conditions. *Dokl. Phys. Chem.* **2010**, *433*, 132–135. [[CrossRef](#)]
49. Iizuka-Oku, R.; Yagi, T.; Gotou, H.; Okuchi, T.; Hattori, T.; Sano-Furukawa, A. Hydrogenation of iron in the early stage of Earth's evolution. *Nat. Commun.* **2017**, *8*, 14096. [[CrossRef](#)]
50. Palyanov, Y.N.; Bataleva, Y.V.; Sokol, A.G.; Borzdov, Y.M.; Kupriyanov, I.N.; Reutsky, V.N.; Sobolev, N.V. Mantle–slab interaction and redox mechanism of diamond formation. *Proc. Natl. Acad. Sci. USA* **2013**, *110*, 20408–20413. [[CrossRef](#)]
51. Stagno, V. Carbon, carbides, carbonates and carbonatitic melts in the Earth's interior. *J. Geol. Soc.* **2019**, *176*, 375–387. [[CrossRef](#)]
52. Luth, R.W. Natural versus experimental control of oxidation state: Effects on the composition and speciation of C–O–H fluids. *Am. Mineral.* **1989**, *74*, 50–57.
53. Sokol, A.G.; Palyanova, G.A.; Palyanov, Y.N.; Tomilenko, A.A.; Melenevsky, V.N. Fluid regime and diamond formation in the reduced mantle: Experimental constraints. *Geochim. Cosmochim. Acta* **2009**, *73*, 5820–5834. [[CrossRef](#)]
54. Palyanov, Y.N.; Borzdov, Y.M.; Khokhryakov, A.F.; Kupriyanov, I.N.; Sokol, A.G. Effect of nitrogen impurity on diamond crystal growth processes. *Cryst. Growth Des.* **2010**, *10*, 3169–3175. [[CrossRef](#)]
55. Sokol, A.G.; Borzdov, Y.M.; Palyanov, Y.N.; Khokhryakov, A.F. High-temperature calibration of a multi-anvil high-pressure apparatus. *High Press. Res.* **2015**, *35*, 139–147. [[CrossRef](#)]
56. Sokol, A.G.; Tomilenko, A.A.; Bul'bak, T.A.; Palyanova, G.A.; Sokol, I.A.; Palyanov, Y.N. Carbon and Nitrogen Speciation in N-poor C–O–H–N Fluids at 6.3 GPa and 1100–1400 °C. *Sci. Rep.* **2017**, *7*, 706. [[CrossRef](#)]
57. Borzdov, Y.; Pal'yanov, Y.; Kupriyanov, I.; Gusev, V.; Khokhryakov, A.; Sokol, A.; Efremov, A. HPHT synthesis of diamond with high nitrogen content from an Fe<sub>3</sub>N–C system. *Diam. Relat. Mater.* **2002**, *11*, 1860–1870. [[CrossRef](#)]
58. Sokol, A.G.; Tomilenko, A.A.; Bul'bak, T.A.; Kruk, A.N.; Zaikin, P.A.; Sokol, I.A.; Seryotkin, Y.V.; Palyanov, Y.N. The Fe–C–O–H–N system at 6.3–7.8 GPa and 1200–1400 °C: Implications for deep carbon and nitrogen cycles. *Contrib. Mineral. Petrol.* **2018**, *173*, 47. [[CrossRef](#)]

59. Sokol, A.G.; Palyanov, Y.N.; Tomilenko, A.A.; Bul'bak, T.A.; Palyanova, G.A. Carbon and nitrogen speciation in nitrogen-rich C–O–H–N fluids at 5.5–7.8 GPa. *Earth Planet. Sci. Lett.* **2017**, *460*, 234–243. [[CrossRef](#)]
60. Zhang, C.; Duan, Z. A model for C–O–H fluid in the Earth's mantle. *Geochim. Cosmochim. Acta* **2009**, *73*, 2089–2102. [[CrossRef](#)]
61. Bataleva, Y.V.; Palyanov, Y.N.; Borzdov, Y.M.; Bayukov, O.A.; Zdrokov, E.V. Iron carbide as a source of carbon for graphite and diamond formation under lithospheric mantle P–T parameters. *Lithos* **2017**, *286–287*, 151–161. [[CrossRef](#)]
62. Robertson, A.J.B. The Pyrolysis of Methane, Ethane and n-butane on a Platinum Filament. *Proc. R. Soc. Lond. Ser. A Math. Phys. Eng. Sci.* **1949**, *199*, 394–411.
63. Belgued, M.; Amariglio, A.; Paréja, P.; Amariglio, H. Oxygen-Free conversion of methane to higher alkanes through an isothermal two-step reaction on platinum (EUROPT-1): II. hydrogenation of the adspecies resulting from the chemisorption of methane. *J. Catal.* **1996**, *159*, 449–457. [[CrossRef](#)]
64. Sverjensky, D.A.; Stagno, V.; Huang, F. Important role for organic carbon in subduction-zone fluids in the deep carbon cycle. *Nat. Geosci.* **2014**, *7*, 909. [[CrossRef](#)]
65. Cimino, A.; Boudart, M.; Taylor, H. Ethane hydrogenation-cracking on iron catalysts with and without alkali. *J. Phys. Chem.* **1954**, *58*, 796–800. [[CrossRef](#)]
66. Hasterok, D.; Chapman, D.S. Heat production and geotherms for the continental lithosphere. *Earth Planet. Sci. Lett.* **2011**, *307*, 59–70. [[CrossRef](#)]
67. Syracuse, E.M.; van Keken, P.E.; Abers, G.A. The global range of subduction zone thermal models. *Phys. Earth Planet. Inter.* **2010**, *183*, 73–90. [[CrossRef](#)]
68. Huizenga, J.M.; Crossingham, A.; Viljoen, F. Diamond precipitation from ascending reduced fluids in the Kaapvaal lithosphere: Thermodynamic constraints. *C. R. Geosci.* **2012**, *344*, 67–76. [[CrossRef](#)]
69. Sokol, A.G.; Tomilenko, A.A.; Bul'bak, T.A.; Kruk, A.N.; Sokol, I.A.; Palyanov, Y.N. Fate of fluids at the base of subcratonic lithosphere: Experimental constraints at 5.5–7.8 GPa and 1150–1350 °C. *Lithos* **2018**, *318*, 419–433. [[CrossRef](#)]
70. Thomassot, E.; Cartigny, P.; Harris, J.W.; (Fanus) Viljoen, K.S. Methane-related diamond crystallization in the Earth's mantle: Stable isotope evidences from a single diamond-bearing xenolith. *Earth Planet. Sci. Lett.* **2007**, *257*, 362–371. [[CrossRef](#)]
71. Shirey, S.B.; Pearson, D.G.; Walter, M.J.; Aulbach, S.; Brenker, F.E.; Bureau, H.; Burnham, A.D.; Cartigny, P.; Chacko, T.; Frost, D.J.; et al. Diamonds and the Mantle Geodynamics of Carbon: Deep Mantle Carbon Evolution from the Diamond Record. In *Deep Carbon: Past to Present*; Orcutt, B., Daniel, I., Dasgupta, R., Eds.; Cambridge University Press: Cambridge, UK, 2019; pp. 89–128.
72. Frezzotti, M.L. Diamond growth from organic compounds in hydrous fluids deep within the Earth. *Nat. Commun.* **2019**, *10*, 4952. [[CrossRef](#)]
73. Tappe, S.; Foley, S.F.; Kjarsgaard, B.A.; Romer, R.L.; Heaman, L.M.; Stracke, A.; Jenner, G.A. Between carbonatite and lamproite—Diamondiferous Torngat ultramafic lamprophyres formed by carbonate-fluxed melting of cratonic MARID-type metasomes. *Geochim. Cosmochim. Acta* **2008**, *72*, 3258–3286. [[CrossRef](#)]
74. Hearnlund, J.; Leinenweber, K.; Locke, D.; Tyburczy, J. A numerical model for steady-state temperature distributions in solid-medium high-pressure cell assemblies. *Am. Mineral.* **2006**, *91*, 295–305. [[CrossRef](#)]

